This is an author's version of an article published in the *QUARTERLY JOURNAL OF THE ROYAL METEOROLOGICAL SOCIETY*:
Q. J. R. Meteorol. Soc. **133**: 595–605 (2007)
This work was first published by John Wiley & Sons, Ltd. at www.interscience.wiley.com
The definitive version of this work may be obtained from Wiley Interscience: http://dx.doi.org/10.1002/qj.49

On the distribution of subsidence in the hurricane eye

Wayne H. Schubert,[a]* Christopher M. Rozoff,[a] Jonathan L. Vigh,[a] Brian D. McNoldy[a] and James P. Kossin[b]

[a]*Colorado State University, USA*
[b]*University of Wisconsin, Madison, USA*

ABSTRACT: Two hurricane eye features that have yet to be adequately explained are the clear-air moat that forms at the outer edge of the eye and the hub cloud that forms near the circulation centre. To investigate whether these features can be explained by the spatial distribution of the subsidence field, we have derived an analytical solution of the Sawyer–Eliassen transverse circulation equation for a three-region approximation with an unforced central eye region of intermediate or high inertial stability, a diabatically-forced eyewall region of high inertial stability, and an unforced far-field of low inertial stability. This analytical solution isolates the conditions under which the subsidence is concentrated near the edge of the eye. The crucial parameter is the dimensionless dynamical radius of the eye, defined as the physical radius of the eye divided by the characteristic Rossby length in the eye. When this dimensionless dynamical radius is less than 0.6, there is less than 10% horizontal variation in the subsidence rate across the eye; when it is greater than 1.8, the subsidence rate at the edge of the eye is more than twice as strong as at the centre of the eye. When subsidence is concentrated at the edge of the eye, the largest temperature anomalies occur near there rather than at the vortex centre. This warm-ring structure, as opposed to a warm-core structure, is often observed in the lower troposphere of intense hurricanes. Copyright © 2007 Royal Meteorological Society

KEY WORDS eyewall; hub cloud; moat

Received 1 September 2006; Revised 2 February 2007; Accepted 6 February 2007

1. Introduction

In reviewing the findings of early hurricane reconnaissance flights, Simpson and Starrett (1955) presented the schematic reproduced here as Figure 1. They emphasized the fact that the hurricane eye often contains low-level stratocumulus, which takes the form of a 'hub cloud' near the circulation centre, surrounded by a 'moat' of clear air or thin stratocumulus near the outer edge of the eye. In recent literature, the term 'moat' has been used to describe the radar-echo-free region between the primary eyewall and a concentric eyewall at larger radius. Our discussion here is limited to the original Simpson–Starrett moat (or inner moat), as opposed to the outer moat that occurs between concentric eyewalls. The inner-moat structure has been confirmed by several later studies. For example, Bundgaard (1958) and Fletcher *et al.* (1961) presented U-2 photographs taken from the lower stratosphere looking down on the eyes of Typhoon Kit (14 November 1957) and Typhoon Ida (25 September 1958). One of the Ida photographs, taken just after rapid deepening to 877 hPa (Jordan, 1959), is reproduced here as Figure 2. It shows low-level stratocumulus in the eye, with cloud tops near 2250 m. Of particular interest is the moat of cloud-free air at the edge of the eye, which is consistent with the Simpson–Starrett schematic. Bundgaard's interpretation of such features was that 'downdraughts of hot air had gouged out these moats at the eyewall's very edge'.

By 1958, aircraft instrumentation and data-recording technology had advanced to a state where it was possible to obtain data from three aircraft operating simultaneously at different levels in Hurricane Cleo. Based on these data, LaSeur and Hawkins (1963) constructed the temperature anomaly cross-section reproduced here as Figure 3. At this time Cleo had maximum winds of 46 m s^{-1} at a radius of 38 km (21 nautical miles). A striking feature revealed by Figure 3 is that the warmest temperatures in the eye at middle and lower levels occur in a ring at the outer edge of the eye. The figure also suggests a transition from a lower-tropospheric warm-ring structure to an upper-tropospheric warm-core structure.

With the amount of aircraft reconnaissance data accumulated during the 1960s, it became possible to perform composite analyses. A particularly insightful study was that of Gray and Shea (1973), who produced a 21-storm composite analysis of the hurricane inner core region. Their composite vertical motion diagram, reproduced here as the top panel in Figure 4, shows a couplet of strong upward and downward motion with the peak downdraught located just inside the main updraught core. As a summary of their composite analysis, Gray and Shea noted that the largest upward motions occur very close to the radius of maximum wind and that the highest temperatures occur just inside the eyewall, corresponding to the large subsidence warming that occurs at that radius.

*Correspondence to: Wayne H. Schubert, Department of Atmospheric Science, Colorado State University, Fort Collins, Colorado 80523-1371, USA. E-mail: waynes@atmos.colostate.edu

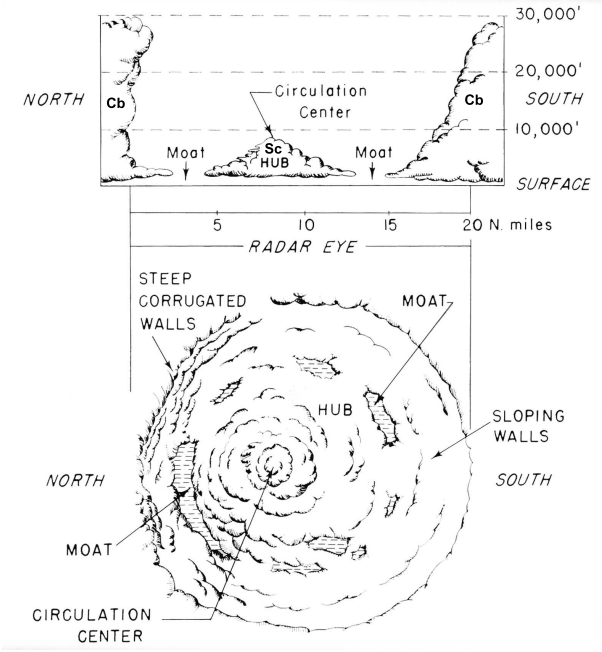

Figure 1. Schematic diagram of the eye of Hurricane Edna, 9–10 September 1954. Of particular interest is the 'hub' cloud near the circulation centre and the clear 'moat' at the edge of the eye. Adapted from Simpson and Starrett (1955).

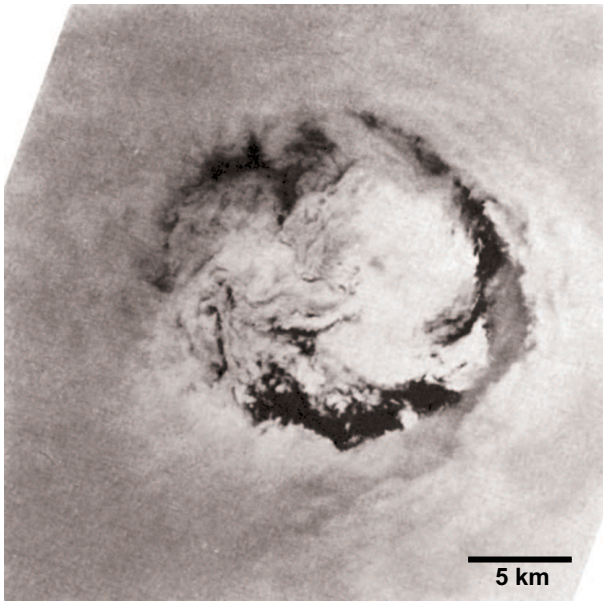

Figure 2. U-2 photograph looking down from the lower stratosphere on the eye of Typhoon Ida, 25 September 1958. The moat of clear air at the edge of the eye is indicative of the strong subsidence there. Adapted from Fletcher *et al.* (1961).

After acquisition of the two NOAA WP-3D aircraft in the late 1970s, it became possible to kinematically compute vertical velocity from more accurate aircraft measurements of the horizontal motion, provided that coordinated radial profiles at several heights were obtained. Based on Hurricane Allen aircraft data (5 August 1980) at the six flight levels shown in the bottom panel of Figure 4, Jorgensen (1984) kinematically computed the mesoscale vertical velocity from radial velocity measurements using the axisymmetric form of the mass continuity equation. His results, shown as isolines of the physical-space vertical velocity, indicate a 10 km-wide eyewall updraught with 7 m s^{-1} peak upward motion and a confined region of 3 m s^{-1} downdraughts just inside the eyewall.

Some recent three-dimensional nested-grid simulations have used horizontal grid spacing capable of resolving the eye structures discussed above. One example is a nested-grid simulation of Hurricane Andrew (1992) produced by Yau *et al.* (2004) using an inner grid with 2 km horizontal spacing. A radial-height section of the azimuthally-averaged vertical velocity (their figure 6a, not reproduced here), at a time when the simulated hurricane had low-level winds of approximately 70 m s^{-1}, revealed an eyewall updraught of 3.5 m s^{-1} at $z = 7$ km and a deep, narrow downdraught along the inner edge of the eyewall. Malkus (1958) and Zhang *et al.* (2002) have emphasized the role that evaporative and sublimative cooling may play in producing such deep, narrow downdraughts. In contrast, the argument presented in this paper ignores such cooling effects in order to isolate other purely dynamical aspects of the problem.

The purpose of this paper is to present a simple theoretical argument that isolates the conditions under which the subsidence and the warmest temperature anomalies are concentrated near the outer edge of the eye. The theoretical argument is based on the balanced vortex model and, in particular, on the associated Sawyer–Eliassen transverse circulation equation (e.g., Ooyama, 1969; Shapiro and Willoughby, 1982; Schubert and Hack, 1982). This argument complements previous studies (e.g., Malkus, 1958; Kuo, 1959; Smith, 1980; Emanuel, 1997; Willoughby, 1998) that did not explicitly used the transverse circulation equation. The paper is organized as follows. The balanced vortex model is presented in Section 2. In Section 3, idealized solutions of the transverse circulation equation are derived. These solutions illustrate how the downward mass flux in the eye depends on the eyewall geometry and the radial distribution of inertial stability. Section 4 presents general numerical solutions of the transverse circulation equation, in order to evaluate results derived from the more strict assumptions in Section 3. Observations of two intense hurricanes, Guillermo and Isabel, which show striking evidence of a warm-ring structure associated with strong subsidence at the outer edge of the eye, are presented in Section 5. A summary of the results and conclusions is given in Section 6.

2. The balanced vortex model

We consider inviscid, axisymmetric, quasi-static, gradient-balanced motions of a stratified, compressible atmosphere on an f-plane. As the vertical coordinate we use $z = H \log(p_0/p)$, where $H = RT_0/g$ is the constant scale height, and where p_0 and T_0 are constant reference values of pressure and temperature. We choose $p_0 = 100$ kPa and $T_0 = 300$ K, the latter of which yields

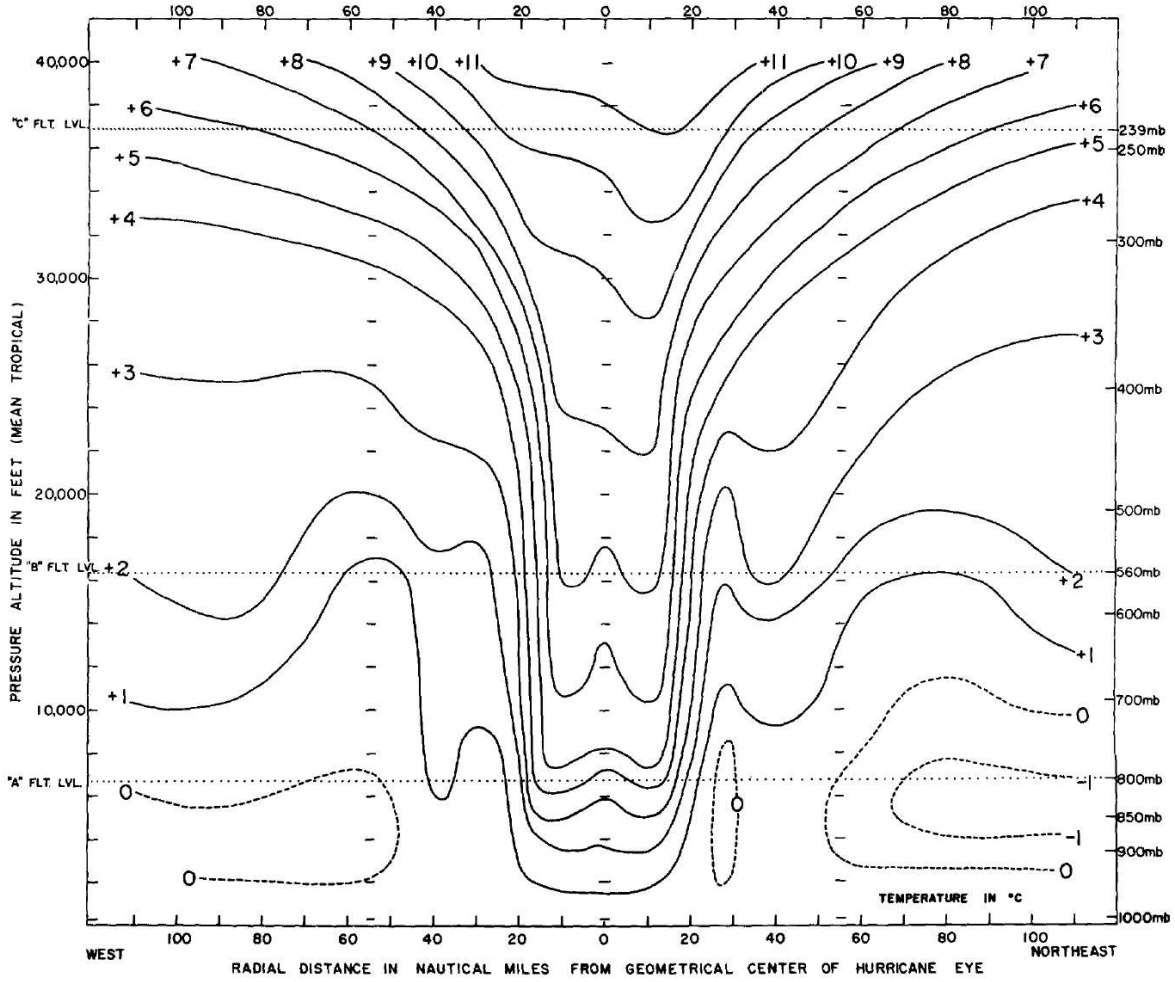

Figure 3. Vertical cross-section of the temperature anomaly (relative to the mean tropical atmosphere profile) along a three-aircraft traversal of Hurricane Cleo (1958). The radius of maximum wind is approximately 38 km (21 nautical miles). On isobaric surfaces below the mid-troposphere, the warmest temperatures occur in a ring at the outer edge of the eye. Adapted from LaSeur and Hawkins (1963).

$H \approx 8.79\,\mathrm{km}$. The governing equations for the balanced vortex model are:

$$\left.\begin{aligned} \left(f+\frac{v}{r}\right)v &= \frac{\partial\phi}{\partial r} \\ \frac{\mathrm{D}v}{\mathrm{D}t}+\left(f+\frac{v}{r}\right)u &= 0 \\ \frac{\partial\phi}{\partial z} &= \frac{g}{T_0}T \\ \frac{\partial(ru)}{r\partial r}+\frac{\partial w}{\partial z}-\frac{w}{H} &= 0 \\ c_\mathrm{p}\frac{\mathrm{D}T}{\mathrm{D}t}+\frac{RT}{H}w &= Q \end{aligned}\right\}, \tag{1}$$

where u and v are the radial and azimuthal components of velocity, $w = \mathrm{D}z/\mathrm{D}t$ is the 'log-pressure vertical velocity', ϕ is the geopotential, f is the constant Coriolis parameter, c_p is the specific heat of dry air at constant pressure, Q is the diabatic heating, and

$$\frac{\mathrm{D}}{\mathrm{D}t} = \frac{\partial}{\partial t}+u\frac{\partial}{\partial r}+w\frac{\partial}{\partial z}$$

is the material derivative.

The thermal wind equation, derived from the gradient and hydrostatic equations, is

$$\left(f+\frac{2v}{r}\right)\frac{\partial v}{\partial z} = \frac{g}{T_0}\frac{\partial T}{\partial r}.$$

Taking $\partial/\partial t$ of this equation, we obtain:

$$\frac{\partial}{\partial z}\left\{\left(f+\frac{2v}{r}\right)\frac{\partial v}{\partial t}\right\} = \frac{g}{T_0}\frac{\partial}{\partial r}\left(\frac{\partial T}{\partial t}\right). \tag{2}$$

This shows that the tendencies $\partial v/\partial t$ and $\partial T/\partial t$ are related by the constraint of continuous thermal wind balance. The diagnostic equation for the transverse circulation is obtained by eliminating the local time derivatives in the tangential wind equation and the thermodynamic equation using Equation (2). To accomplish this, we first note that, because of the continuity equation, the transverse circulation (u, w) can be expressed in terms of the single streamfunction variable ψ, so that

$$\left.\begin{aligned} e^{-z/H}u &= -\frac{\partial\psi}{\partial z} \\ e^{-z/H}w &= \frac{\partial(r\psi)}{r\partial r} \end{aligned}\right\}.$$

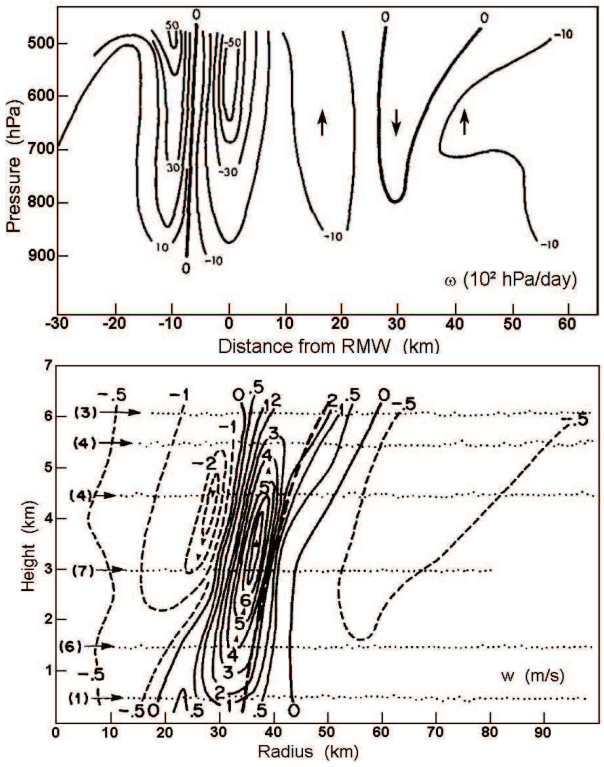

Figure 4. The top panel, adapted from Gray and Shea (1973), displays isolines of the vertical p-velocity, composited with respect to the radius of maximum wind. The bottom panel, adapted from Jorgensen (1984), displays isolines of the physical-space vertical velocity for Hurricane Allen (5 August 1980). In both diagrams the vertical velocity has been computed kinematically from aircraft measurements of radial wind.

We next multiply the tangential wind equation by $-(f + 2v/r)$ and the thermodynamic equation by g/T_0, and write the resulting equations as

$$-\left(f + \frac{2v}{r}\right)\frac{\partial v}{\partial t} + B\frac{\partial(r\psi)}{r\partial r} + C\frac{\partial \psi}{\partial z} = 0, \quad (3)$$

and

$$\frac{g}{T_0}\frac{\partial T}{\partial t} + A\frac{\partial(r\psi)}{r\partial r} + B\frac{\partial \psi}{\partial z} = \frac{g}{c_p T_0}Q, \quad (4)$$

where the static stability A, the baroclinity B and the inertial stability C are defined by

$$A = e^{z/H}\frac{g}{T_0}\left(\frac{\partial T}{\partial z} + \frac{\kappa T}{H}\right), \quad (5)$$

$$B = -e^{z/H}\left(f + \frac{2v}{r}\right)\frac{\partial v}{\partial z} = -e^{z/H}\frac{g}{T_0}\frac{\partial T}{\partial r}, \quad (6)$$

$$C = e^{z/H}\left(f + \frac{2v}{r}\right)\left(f + \frac{\partial(rv)}{r\partial r}\right). \quad (7)$$

Adding $\partial/\partial r$ of Equation (4) to $\partial/\partial z$ of Equation (3), and then using Equation (2), we obtain the Sawyer–Eliassen transverse circulation equation:

$$\frac{\partial}{\partial r}\left(A\frac{\partial(r\psi)}{r\partial r} + B\frac{\partial \psi}{\partial z}\right) + \frac{\partial}{\partial z}\left(B\frac{\partial(r\psi)}{r\partial r} + C\frac{\partial \psi}{\partial z}\right) = \frac{g}{c_p T_0}\frac{\partial Q}{\partial r}. \quad (8)$$

We shall only consider vortices with $AC - B^2 > 0$ everywhere, in which case Equation (8) is an elliptic equation. As for boundary conditions on Equation (8), we require that ψ vanish at $r = 0$ and at the bottom and top isobaric surfaces $z = 0$, $z = z_T$, and that $r\psi \to 0$ as $r \to \infty$. In the next section we solve a simplified version of Equation (8) under these boundary conditions.

3. Solutions of the transverse circulation equation

For real hurricanes the coefficients A, B and C can have complicated spatial distributions, which would preclude analytical solution of Equation (8). To obtain analytical solutions, we shall consider an idealized vortex that leads to a drastic simplification of the coefficients A and B, but retains the crucial radial dependence of the inertial stability C. Thus, we consider a barotropic vortex ($B = 0$), noting that this assumption means that the radial derivative of T on isobaric surfaces is zero, but that, with a cyclonic vortex, the radial derivative of T on physical height surfaces is slightly positive. The static stability is given by

$$A = e^{z/H}N^2,$$

where the square of the Brunt–Väisälä frequency, N^2, is a constant. The inertial stability (Equation 7) can then be written in the form

$$C = e^{z/H}\hat{f}^2,$$

where

$$\hat{f}(r) = \left\{\left(f + \frac{2v}{r}\right)\left(f + \frac{\partial(rv)}{r\partial r}\right)\right\}^{\frac{1}{2}},$$

is the 'effective Coriolis parameter'. Under the above assumptions, (Equation (8)) reduces to

$$N^2\frac{\partial}{\partial r}\left(\frac{\partial(r\psi)}{r\partial r}\right) + \hat{f}^2 e^{-z/H}\frac{\partial}{\partial z}\left(e^{z/H}\frac{\partial \psi}{\partial z}\right) = \frac{g e^{-z/H}}{c_p T_0}\frac{\partial Q}{\partial r}. \quad (9)$$

Assuming that the diabatic heating $Q(r, z)$ and the streamfunction $\psi(r, z)$ have the separable forms

$$Q(r, z) = \hat{Q}(r)\exp\left(\frac{z}{2H}\right)\sin\left(\frac{\pi z}{z_T}\right),$$

$$\psi(r, z) = \hat{\psi}(r)\exp\left(-\frac{z}{2H}\right)\sin\left(\frac{\pi z}{z_T}\right),$$

the partial differential equation (9) reduces to the ordinary differential equation:

$$r^2\frac{d^2\hat{\psi}}{dr^2} + r\frac{d\hat{\psi}}{dr} - (\mu^2 r^2 + 1)\hat{\psi} = \frac{g r^2}{c_p T_0 N^2}\frac{d\hat{Q}}{dr}, \quad (10)$$

where

$$\mu^2 = \frac{\hat{f}^2}{N^2}\left\{\frac{\pi^2}{z_T^2} + \frac{1}{(2H)^2}\right\}$$

is the inverse Rossby length squared. Here we are particularly interested in the important role played by radial variations of $\hat{f}$, and hence radial variations of μ. To treat radial variations of $\hat{f}$ and μ in a simple manner, we consider the specific barotropic vortex in which the azimuthal wind is given by the following formulae:

- If $0 \le r \le r_1$ (eye):

$$2rv(r) = \left(\hat{f}_0 - f\right) r^2. \tag{11}$$

- If $r_1 \le r \le r_2$ (eyewall):

$$2rv(r) = \left\{\hat{f}_0^2 r_1^4 + \hat{f}_1^2 \left(r^4 - r_1^4\right)\right\}^{\frac{1}{2}} - fr^2. \tag{12}$$

- If $r_2 \le r < \infty$ (far-field):

$$2rv(r) = \left\{\hat{f}_0^2 r_1^4 + \hat{f}_1^2 \left(r_2^4 - r_1^4\right) + \hat{f}_2^2 \left(r^4 - r_2^4\right)\right\}^{\frac{1}{2}} - fr^2. \tag{13}$$

Here r_1 and r_2 are specified constants giving the inner and outer radii of the eyewall. From Equations (11)–(13) we can easily show that

$$\hat{f}(r) = \left\{\left(f + \frac{2v}{r}\right)\left(f + \frac{\partial(rv)}{r\partial r}\right)\right\}^{\frac{1}{2}} = \begin{cases} \hat{f}_0 & \text{if } 0 \le r < r_1 \text{ (eye)} \\ \hat{f}_1 & \text{if } r_1 < r < r_2 \text{ (eyewall)} \\ \hat{f}_2 & \text{if } r_2 < r < \infty \text{ (far-field)} \end{cases}, \tag{14}$$

so that $\hat{f}_0$, $\hat{f}_1$ and $\hat{f}_2$ can be interpreted as specified constants giving the effective Coriolis parameters in the eye, eyewall, and far-field. Because of Equation (14), the inverse Rossby length $\mu(r)$ also has the piecewise-constant form:

$$\mu(r) = \frac{\hat{f}(r)}{N}\left(\frac{\pi^2}{z_T^2} + \frac{1}{4H^2}\right)^{\frac{1}{2}} = \begin{cases} \mu_0 & \text{if } 0 \le r < r_1 \text{ (eye)} \\ \mu_1 & \text{if } r_1 < r < r_2 \text{ (eyewall)} \\ \mu_2 & \text{if } r_2 < r < \infty \text{ (far-field)} \end{cases}, \tag{15}$$

where the constants μ_0, μ_1 and μ_2 are defined in terms of the constants $\hat{f}_0$, $\hat{f}_1$ and $\hat{f}_2$ through Equation (14) and the second equality in Equation (15). Plots of $v(r)$, computed from Equations (11)–(13) using the parameters listed in Table I, are shown in Figure 5(a). In constructing this table and this figure we have used $f = 5 \times 10^{-5}\,\mathrm{s}^{-1}$ and

$$\frac{N}{f}\left\{\frac{\pi^2}{z_T^2} + \frac{1}{4H^2}\right\}^{-\frac{1}{2}} = 1000\,\mathrm{km}.$$

Note that the four $v(r)$ profiles, denoted by cases A–D, all have $v(r_2) = 70\,\mathrm{m\,s}^{-1}$. Cases B and D are U-shaped, so that there is relatively high vorticity in the eyewall and relatively low vorticity in the eye. In contrast, cases A and C are Rankine-like, with equal vorticity in the eye and eyewall. The Rossby length in the eye, given by μ_0^{-1} and listed in the seventh column of the table, is small for the Rankine-like vortices A and C. As a consequence, the (dimensionless) dynamical size of the eye, given by $\mu_0 r_1$ and listed in the eighth column, is large for the Rankine-like vortices A and C, whereas it is small for the U-shaped vortices B and D. In a crude sense, the Rankine-like profiles A and C can be envisioned as having evolved respectively from the U-shaped profiles B and D via potential vorticity mixing (Schubert *et al.*, 1999; Kossin and Eastin, 2001; Kossin and Schubert, 2001; Kossin *et al.*, 2002; Montgomery *et al.*, 2002). Note that in the transformations B → A and D → C, the physical radius of the eye does not change but the dynamical radius of the eye increases by more than a factor of three for B → A and by nearly a factor of five for D → C. This effect is crucial in later discussions.

We now assume that the diabatic heating has the piecewise-constant form

$$\hat{Q}(r) = \begin{cases} 0 & \text{if } 0 \le r < r_1 \text{ (eye)} \\ Q_1 & \text{if } r_1 < r < r_2 \text{ (eyewall)} \\ 0 & \text{if } r_2 < r < \infty \text{ (far-field)} \end{cases}, \tag{16}$$

where Q_1 is a constant. This structure represents the heating that occurs when moist updraughts are confined to an annular eyewall. Only two of the three parameters r_1, r_2 and Q_1 are independently varied. The three parameters are constrained by:

$$\frac{Q_1}{c_p}\left(r_2^2 - r_1^2\right) = 125\,\mathrm{K\ day}^{-1}\,(50\,\mathrm{km})^2. \tag{17}$$

A crude interpretation of this constraint is that the implied area-averaged rainfall is fixed as we vary any two of the three parameters r_1, r_2 and Q_1. Such latent heating rates are supported by the satellite-derived measurements of Rodgers *et al.* (1998).

Because of Equation (16), the right-hand side of Equation (10) vanishes everywhere except at the points $r = r_1$

Table I. Vortex parameters: radius of inner edge of eyewall (r_1); radius of outer edge of eyewall (r_2); effective Coriolis parameter in eye ($\hat{f}_0/f$), eyewall ($\hat{f}_1/f$), and far-field ($\hat{f}_2/f$); Rossby length in eye (μ_0^{-1}); dynamic radius of eye ($\mu_0 r_1$); proportion of downward mass flux occurring in eye (η).

Case	r_1 (km)	r_2 (km)	$\hat{f}_0/f$	$\hat{f}_1/f$	$\hat{f}_2/f$	μ_0^{-1} (km)	$\mu_0 r_1$	η (%)
A	10	20	141.0	141.0	1.0	7.1	1.41	12.6
B	10	20	41.0	145.2	1.0	24.4	0.41	14.7
C	30	40	71.0	71.0	1.0	14.1	2.13	13.5
D	30	40	14.3	85.3	1.0	69.9	0.43	21.1

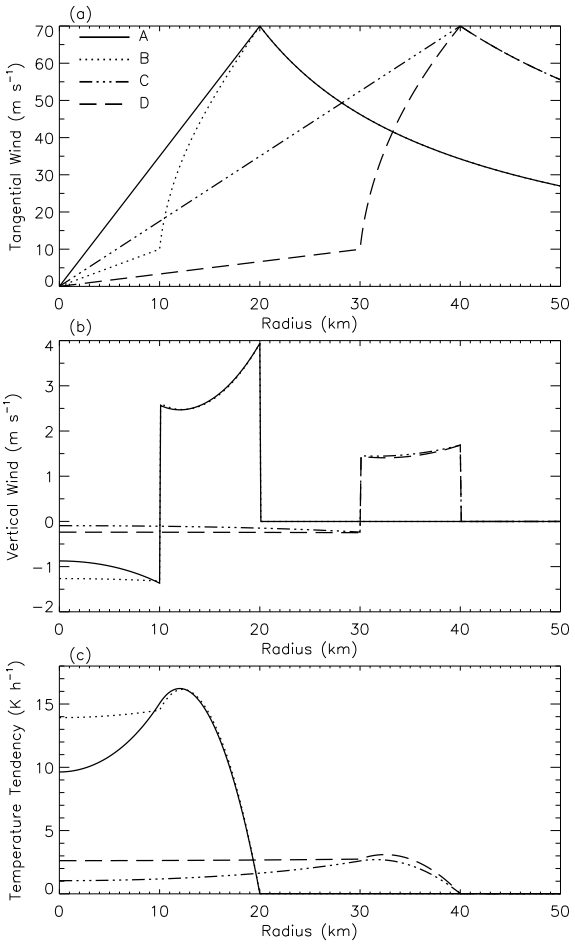

Figure 5. (a) Plots of $v(r)$, computed from Equations (11)–(13), using the parameter values listed in Table I. (b) Corresponding radially-dependent part of vertical log-pressure velocities given by Equation (24). (c) Corresponding temperature tendencies obtained from Equations (25)–(27).

and $r = r_2$. At these points, the differential equation (10) is replaced by the two jump conditions

$$\left.\begin{aligned} \left[\frac{\mathrm{d}(r\hat{\psi})}{r\,\mathrm{d}r}\right]_{r_1^-}^{r_1^+} &= \frac{g\,Q_1}{c_\mathrm{p}\,T_0\,N^2} \\ \left[\frac{\mathrm{d}(r\hat{\psi})}{r\,\mathrm{d}r}\right]_{r_2^-}^{r_2^+} &= -\frac{g\,Q_1}{c_\mathrm{p}\,T_0\,N^2} \end{aligned}\right\}, \tag{18}$$

which can be derived by integrating Equation (10) across narrow intervals straddling the points $r = r_1$ and $r = r_2$. Assuming Equation (16), the solution of the ordinary differential equation (10) consists of linear combinations of the first-order modified Bessel functions $\mathrm{I}_1(\mu r)$ and $\mathrm{K}_1(\mu r)$ in each of the three regions. These modified Bessel functions are shown by the dashed curves in Figure 6. Because our boundary condition requires that $\hat{\psi} = 0$ at $r = 0$, we can discard the $\mathrm{K}_1(\mu r)$ solution in the inner region. Similarly, because $r\hat{\psi} \to 0$ as $r \to \infty$, we can discard the $\mathrm{I}_1(\mu r)$ solution in the outer region.

The solution of Equation (10) can then be written as

$$\hat{\psi}(r) = \begin{cases} \hat{\psi}_1 \dfrac{\mathrm{I}_1(\mu_0 r)}{\mathrm{I}_1(\mu_0 r_1)} & 0 \le r \le r_1 \\ \dfrac{\hat{\psi}_1 F(r, r_2) + \hat{\psi}_2 F(r_1, r)}{F(r_1, r_2)} & r_1 \le r \le r_2 \\ \hat{\psi}_2 \dfrac{\mathrm{K}_1(\mu_2 r)}{\mathrm{K}_1(\mu_2 r_2)} & r_2 \le r < \infty \end{cases}, \tag{19}$$

where

$$F(x, y) = \mathrm{I}_1(\mu_1 x)\,\mathrm{K}_1(\mu_1 y) - \mathrm{K}_1(\mu_1 x)\,\mathrm{I}_1(\mu_1 y)$$

and $\hat{\psi}_1$ and $\hat{\psi}_2$ are constants to be determined by the two jump conditions (18). Note that Equation (19) guarantees that $\hat{\psi}(r)$ is continuous at $r = r_1$ and $r = r_2$.

The vertical motion field can be obtained from the streamfunction (Equation (19)) via differentiation, using the relations

$$\left.\begin{aligned} \frac{\mathrm{d}\{r\mathrm{I}_1(\mu r)\}}{r\mathrm{d}r} &= \mu \mathrm{I}_0(\mu r) \\ \frac{\mathrm{d}\{r\mathrm{K}_1(\mu r)\}}{r\mathrm{d}r} &= -\mu \mathrm{K}_0(\mu r) \end{aligned}\right\},$$

where $\mathrm{I}_0(\mu r)$ and $\mathrm{K}_0(\mu r)$ are the zeroth-order modified Bessel functions (shown by the solid curves in Figure 6). Thus, from differentiation of Equation (19) we obtain:

$$\frac{\mathrm{d}(r\hat{\psi})}{r\,\mathrm{d}r} = \begin{cases} \hat{\psi}_1 \mu_0 \dfrac{\mathrm{I}_0(\mu_0 r)}{\mathrm{I}_1(\mu_0 r_1)} & 0 \le r < r_1 \\ \dfrac{\hat{\psi}_1 \mu_1 G(r, r_2) - \hat{\psi}_2 \mu_1 G(r, r_1)}{F(r_1, r_2)} & r_1 < r < r_2 \\ -\hat{\psi}_2 \mu_2 \dfrac{\mathrm{K}_0(\mu_2 r)}{\mathrm{K}_1(\mu_2 r_2)} & r_2 < r < \infty \end{cases}, \tag{20}$$

where

$$G(x, y) = \mathrm{I}_0(\mu_1 x)\,\mathrm{K}_1(\mu_1 y) + \mathrm{K}_0(\mu_1 x)\,\mathrm{I}_1(\mu_1 y).$$

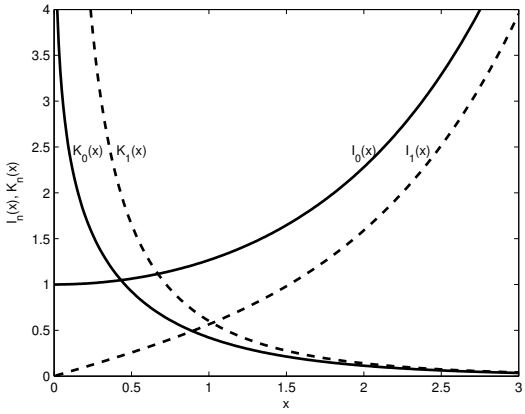

Figure 6. The first-order modified Bessel functions $\mathrm{I}_1(x)$ and $\mathrm{K}_1(x)$, from which the streamfunction is constructed, and the zeroth-order modified Bessel functions $\mathrm{I}_0(x)$ and $\mathrm{K}_0(x)$, from which the vertical motion is constructed.

Use of Equation (20) in the jump conditions (18) leads to two algebraic equations that determine the constants $\hat{\psi}_1$ and $\hat{\psi}_2$. Solving these two algebraic equations, and with the aid of the Wronskian

$$\mathrm{I}_0(x)\,\mathrm{K}_1(x) + \mathrm{K}_0(x)\,\mathrm{I}_1(x) = \frac{1}{x},$$

we can express $\hat{\psi}_1$ and $\hat{\psi}_2$ as

$$\left.\begin{aligned} \hat{\psi}_1 &= \frac{g Q_1 r_2 F(r_1, r_2)}{c_\mathrm{p} T_0 N^2}\left(\frac{1-\alpha}{1-\alpha\beta}\right) \\ \hat{\psi}_2 &= \frac{g Q_1 r_1 F(r_1, r_2)}{c_\mathrm{p} T_0 N^2}\left(\frac{\beta-1}{1-\alpha\beta}\right) \end{aligned}\right\}, \tag{21}$$

where

$$\alpha = \mu_1 r_1 \left\{ G(r_2, r_1) - F(r_1, r_2)\frac{\mu_2 \mathrm{K}_0(\mu_2 r_2)}{\mu_1 \mathrm{K}_1(\mu_2 r_2)} \right\}, \tag{22}$$

and

$$\beta = \mu_1 r_2 \left\{ G(r_1, r_2) - F(r_1, r_2)\frac{\mu_0 \mathrm{I}_0(\mu_0 r_1)}{\mu_1 \mathrm{I}_1(\mu_0 r_1)} \right\}. \tag{23}$$

To summarize, the solution of the transverse circulation equation (8), for the barotropic vortex (Equations (11)–(13)) and the diabatic heating (Equation (16)), yields a log-pressure vertical velocity given by:

$$w(r,z) = e^{z/(2H)} \sin\left(\frac{\pi z}{z_T}\right) \times \begin{cases} \hat{\psi}_1 \mu_0 \dfrac{\mathrm{I}_0(\mu_0 r)}{\mathrm{I}_1(\mu_0 r_1)} & 0 \le r < r_1 \\ \hat{\psi}_1 \mu_1 \dfrac{G(r, r_2)}{F(r_1, r_2)} - \hat{\psi}_2 \mu_1 \dfrac{G(r, r_1)}{F(r_1, r_2)} & r_1 < r < r_2 \\ -\hat{\psi}_2 \mu_2 \dfrac{\mathrm{K}_0(\mu_2 r)}{\mathrm{K}_1(\mu_2 r_2)} & r_2 < r < \infty \end{cases}. \tag{24}$$

Plots of the radial dependence on the right-hand side of Equation (24) for cases A–D are shown in Figure 5(b). For the U-shaped vortices B and D, the subsidence rate is nearly uniform in the eye because the dynamic radius of the eye is small (0.41 for B and 0.43 for D) – the centre of the eye is less than a Rossby length from the eyewall. For the Rankine-like vortices A and C, the subsidence rate in the centre of the eye is considerably reduced because the high inertial stability of the eye results in the centre of the eye being more than a Rossby length from the eyewall. From the first line in Equation (24) we can see that, on any isobaric surface, the ratio of the subsidence rate at the edge of the eye to the subsidence rate at the centre of the eye is $\mathrm{I}_0(\mu_0 r_1)$, since $\mathrm{I}_0(0) = 1$. From Figure 6 we note that $\mathrm{I}_0(\mu_0 r_1) < 1.1$ when $\mu_0 r_1 < 0.6$, while $\mathrm{I}_0(\mu_0 r_1) > 2$ when $\mu_0 r_1 > 1.8$. We conclude that there is less than 10% horizontal variation in the subsidence rate in the eye when the eye is dynamically small ($\mu_0 r_1 < 0.6$), whereas the subsidence rate at the edge of the eye is more than twice as strong as the subsidence rate in the centre of the eye when the eye is dynamically large ($\mu_0 r_1 > 1.8$).

It is of interest to calculate the proportion of the upward mass flux in the eyewall that turns inward to subside in the eye and the proportion that turns outward to subside in the far-field. From the streamfunction solution (Equation (19)), the fractional downward mass flux in the eye (on any isobaric surface) can be expressed as

$$\begin{aligned} \eta &= \frac{\text{downward mass flux in eye}}{\text{total downward mass flux}} \\ &= \frac{\displaystyle\int_0^{r_1} w r \,\mathrm{d}r}{\displaystyle\int_0^{r_1} w r \,\mathrm{d}r + \int_{r_2}^{\infty} w r \,\mathrm{d}r} \\ &= \frac{\displaystyle\int_0^{r_1} \frac{\mathrm{d}(r\hat{\psi})}{\mathrm{d}r}\,\mathrm{d}r}{\displaystyle\int_0^{r_1} \frac{\mathrm{d}(r\hat{\psi})}{\mathrm{d}r}\,\mathrm{d}r + \int_{r_2}^{\infty} \frac{\mathrm{d}(r\hat{\psi})}{\mathrm{d}r}\,\mathrm{d}r} \\ &= \frac{r_1\hat{\psi}_1}{r_1\hat{\psi}_1 - r_2\hat{\psi}_2} \\ &= \frac{\alpha - 1}{\alpha + \beta - 2}, \end{aligned}$$

where the final equality follows from the use of Equations (21). From Equations (22) and (23), we see that the value of η depends on the five parameters r_1, r_2, μ_0, μ_1 and μ_2. Values of η for cases A–D are shown in the last column of Table I. Note that the transformations to vortices with high inertial stability cores (i.e. B → A and D → C) lead to a reduction in the proportion of the downward mass flux that occurs in the eye (e.g. 21.1% to 13.5% for D → C). Thus, the reduction of the subsidence rate at the centre of the eye means that the proportion of total downward mass flux that occurs in the eye is reduced.

The temperature tendency implied by the secondary circulation can be obtained from Equation (4) with $B = 0$. After separating off the vertical dependence, we obtain:

$$\frac{\partial \hat{T}}{\partial t} = \frac{\hat{Q}}{c_\mathrm{p}} - \frac{T_0 N^2}{g}\frac{\mathrm{d}(r\hat{\psi})}{r\mathrm{d}r}.$$

Using Equations (16) and (20)–(23), we obtain the following formulae:

- If $0 \le r \le r_1$:

$$\frac{\partial \hat{T}}{\partial t} = \frac{Q_1}{c_\mathrm{p}}\left\{1 - \left(\frac{1-\alpha}{1-\alpha\beta}\right)\mu_1 r_2 G(r_1, r_2) - \left(\frac{1-\beta}{1-\alpha\beta}\right)\right\}\frac{\mathrm{I}_0(\mu_0 r)}{\mathrm{I}_0(\mu_0 r_1)}. \tag{25}$$

- If $r_1 \le r \le r_2$:

$$\frac{\partial \hat{T}}{\partial t} = \frac{Q_1}{c_\mathrm{p}}\left\{1 - \left(\frac{1-\alpha}{1-\alpha\beta}\right)\mu_1 r_2 G(r, r_2) - \left(\frac{1-\beta}{1-\alpha\beta}\right)\mu_1 r_1 G(r, r_1)\right\}. \tag{26}$$

- If $r_2 \le r < \infty$:

$$\frac{\partial \hat{T}}{\partial t} = \frac{Q_1}{c_p}\left\{1 - \left(\frac{1-\alpha}{1-\alpha\beta}\right) - \left(\frac{1-\beta}{1-\alpha\beta}\right)\mu_1 r_1 G(r_2, r_1)\right\}\frac{\mathrm{K}_0(\mu_2 r)}{\mathrm{K}_0(\mu_2 r_2)}. \quad (27)$$

Plots of $\partial\hat{T}/\partial t$, computed from Equations (25)–(27) for cases A–D, are shown in Figure 5(c). Note that in cases A and C (dynamically large eyes) the temperature tendency is more concentrated near the edge of the eye. This is consistent with the formation of a warm-ring structure in storms with dynamically large eyes. Another interesting feature of these plots is the large variation of $\partial\hat{T}/\partial t$ across the eyewall, even though the diabatic heating $\hat{Q}(r)$ is constant across it. This can be interpreted as follows. From Equation (18) and Figure 5(b) it can be seen that the magnitude of the jumps in vertical velocity are the same at $r = r_1$ and $r = r_2$. Thus, with stronger subsidence at the edge of the eye than just outside the eyewall, the upward motion in the eyewall region is larger in its outer part than in its inner part. For example, considering cases A and C, in the outer part of the eyewall region the compensation between the $(T_0 N^2/g)\{\mathrm{d}(r\hat{\psi})/(r\mathrm{d}r)\}$ term and the $\hat{Q}/c_p$ term is nearly complete, while in the inner part of the eyewall region the former of these two terms is only two-thirds of the latter.

4. Numerical solutions

In order to test the limitations of the barotropic vortex assumption that reduces Equation (8) to Equation (9), we produce numerical solutions of Equation (8) using multigrid methods (Fulton *et al.*, 1986; Ciesielski *et al.*, 1986) with fine spatial resolution ($\Delta r = 250$ m and $\Delta z = 187.5$ m). The diabatic heating $Q(r, z)$ has the same spatial structure as that used in Section 3, except that the discontinuities at r_1 and r_2 are replaced by smooth transitions (A cubic interpolation function was used, so that both $Q(r, z)$ and its radial derivative are continuous.) over a radial distance of 3 km. Figure 7 shows the results of two such calculations, one for the barotropic vortex (upper-left panel) and one for the baroclinic vortex (upper-right panel). These two vortices have the same radial profile of v at the lower boundary. The middle and lower panels show the corresponding w and $\partial T/\partial t$ fields, respectively. The middle two panels show that baroclinity increases the height of the vertical velocity maximum and associated temperature tendency. This vertical shift of the maximum w from the barotropic to baroclinic situation occurs because the baroclinic vortex has increased (decreased) static stability at lower (upper) levels and decreased inertial stability at upper levels. The heights of maximum $|w|$ and $\partial T/\partial t$ are also directly proportional to the level of maximum heating, which in the present example is located in the upper troposphere. Finally, it should be pointed out that numerical solutions for U-shaped profiles (not shown) validate the generality of the dependence of the radial distribution of eye subsidence on the radial profile of inertial stability.

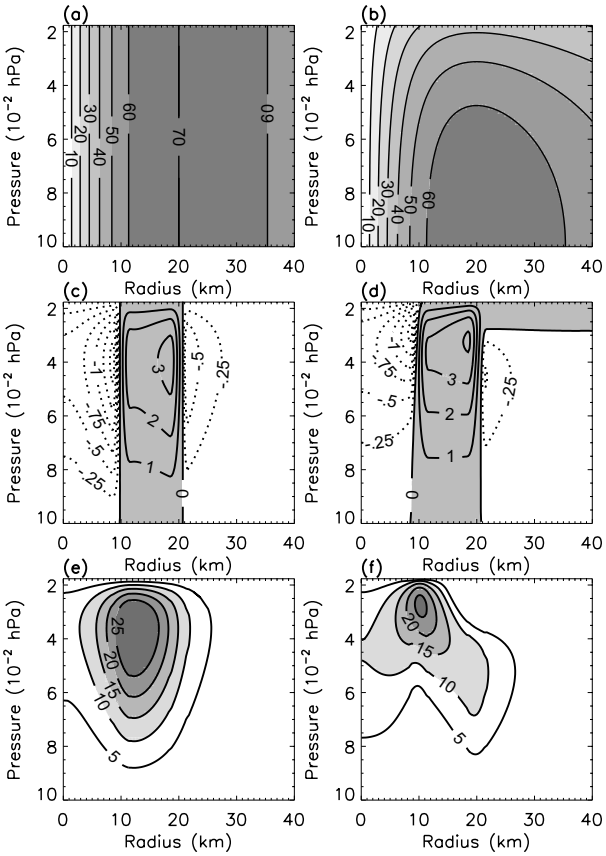

Figure 7. Panels (a) and (b) show $v(r, z)$ for sample barotropic and baroclinic vortices, respectively. Panels (c) and (d) show the corresponding $w(r, z)$ fields, as determined from numerical solution of Equation (8), with a contour interval of 1 m s^{-1} in the ascent regions (solid lines) and -0.25 m s^{-1} in the descent regions (dotted lines). Panels (e) and (f) show the corresponding temperature tendencies $\partial T/\partial t$, with a contour interval of 5 K h^{-1}.

5. Hurricanes Guillermo and Isabel

We now present observations from two intense hurricanes that support the warm-ring structure found in the theoretical arguments of Sections 2 and 3. The first example is from Hurricane Guillermo, a category-4 eastern-Pacific storm that was well observed on 2 and 3 August 1997. Figures 8 (a) and (b) show the time-averaged radial profiles of tangential wind, temperature, and dew-point temperature at 700 hPa for 2 and 3 August, where each composite profile incorporates 18 and 20 passes, respectively. Following Willoughby *et al.* (1982), each flight pass has been interpolated into vortex-centred grids ($\Delta r = 0.5$ km); the data are readily available in such a format from NOAA's Hurricane Research Division. On 2 August, the maximum 700 hPa tangential wind is 52.7 m s^{-1} at $r = 29$ km; on 3 August, the maximum 700 hPa tangential wind is 63.0 m s^{-1} at $r = 26$ km. Thus, Guillermo strengthened

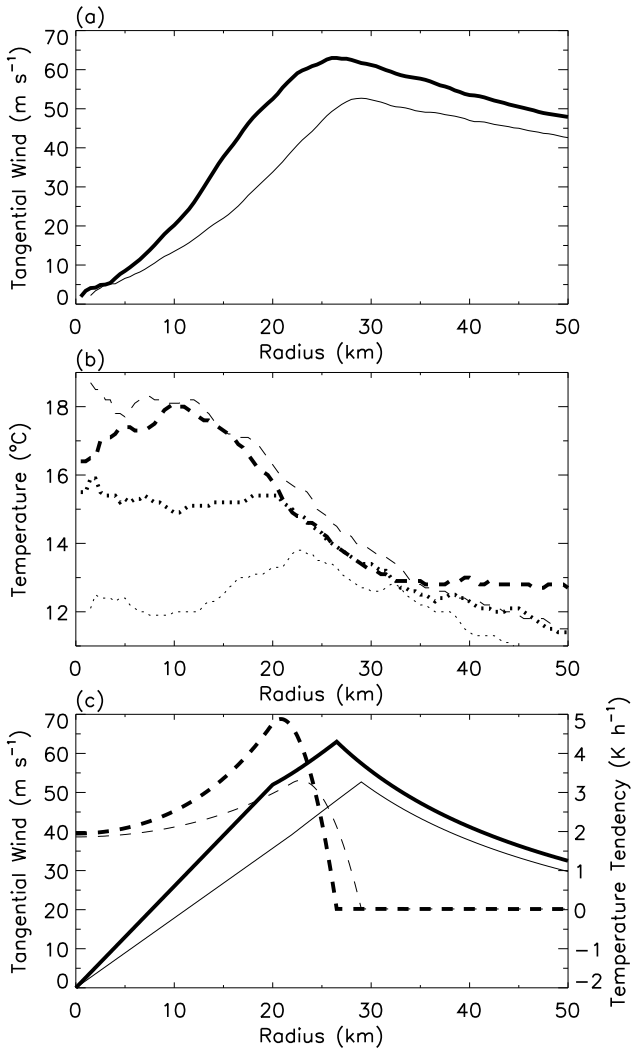

Figure 8. Radial profiles at 700 hPa, from Hurricane Guillermo, of the time-averaged (a) tangential wind on 2 August (light solid line) and 3 August 1997 (heavy solid line), and (b) temperature and dew-point temperature on 2 August (light dashed and dotted lines respectively) and 3 August (heavy dashed and dotted lines respectively). (c) The corresponding three-region model's estimate of Guillermo's 700 hPa tangential wind and temperature tendency on 2 August (light solid and dashed lines respectively) and 3 August (heavy solid and dashed lines respectively).

and its eyewall contracted during this period. A substantial warm-core anomaly of about 5 K persisted (Figure 8(b)), but apparent 'cooling' at $r < 10$ km between the two intensive observational campaigns on 2 and 3 August leads to a warm-ringed structure in the 3 August composite. With a saturated eyewall adjacent to a dew-point depression of 3.2 °C near the inner edge of the eyewall, the 3 August composite is consistent with the results of Sitkowsi *et al.* (2006). On 2 August, the dew-point depression exceeds 6 °C but is uniform across Guillermo's eye.

While admitting the three-region model's inability to capture the U-shaped structure within Guillermo's eye, we can still optimize the three-region model's parameters to estimate the temperature tendencies that should result from the balanced circulation of Guillermo. For 2 August, we choose $r_1 = 22$ km, $r_2 = 29$ km, $v(r_1) = 39.3\,\mathrm{m\,s^{-1}}$, and $v(r_2) = 52.7\,\mathrm{m\,s^{-1}}$; for 3 August, we choose $r_1 = 20$ km, $r_2 = 26.5$ km, $v(r_1) = 52\,\mathrm{m\,s^{-1}}$, and $v(r_2) = 63\,\mathrm{m\,s^{-1}}$. Figure 8(c) shows the estimated tangential wind curves. Incorporating the diabatic heating constraint given by Equation (17) and using Equations (25)–(27), we obtain the temperature tendencies shown by the heavy and light dashed lines in Figure 8(c). On 3 August, there is a greater tendency for the storm to produce a warm-ringed structure. However, the radius of maximum temperature change is offset from the warm-ringed structure observed on 3 August; this may perhaps be explained by the analytical model's simplified vortex geometry, or by its lack of evaporative and sublimative cooling.

Our second observational example is from Hurricane Isabel, a category-5 Atlantic hurricane. Figure 9 is a stunning photograph of the hub cloud in the eye of Isabel on 13 September 2003. On this date, the two NOAA WP-3D aircraft collected high-resolution data from multiple eyewall penetrations at altitudes of 2.1 km and 3.7 km. In Figures 10 (a) and (b), we provide two radial profiles of 1 s flight-level tangential wind at 3.7 km altitude from 1948 UTC to 1956 UTC and at 2.1 km altitude from 1922 UTC to 1931 UTC, respectively. These wind profiles reveal a large outward tilt of the radius of maximum wind (See also the cross-sections shown in Bell and Montgomery (2007).) The associated temperature and dew-point temperature profiles exhibit evidence of subsidence warming and drying inside the eye, particularly near the eyewall. Similar patterns appear in nearly all 16 WP-3D sorties on 13 September. These Isabel results imply that the warm-ring structure can extend over a considerable depth of the lower troposphere. However, it is an open question whether it extends into the upper troposphere or gives way to a warm-core upper tropospheric structure. These Isabel profiles also reveal a vorticity structure more complicated than was specified in the three-region model, which assumed that the eye can be characterized by a single Rossby length. The tangential wind

Figure 9. The eye of Hurricane Isabel on 13 September 2003. The hub cloud (near the centre of the photo) is surrounded by a moat of clear air or thin stratocumulus. Because of the large eye diameter (60–70 km), the eyewall (12–14 km tops) behind the hub clud (3 km top) appears only slightly higher than the hub cloud itself. Photo courtesy of Sim Aberson.

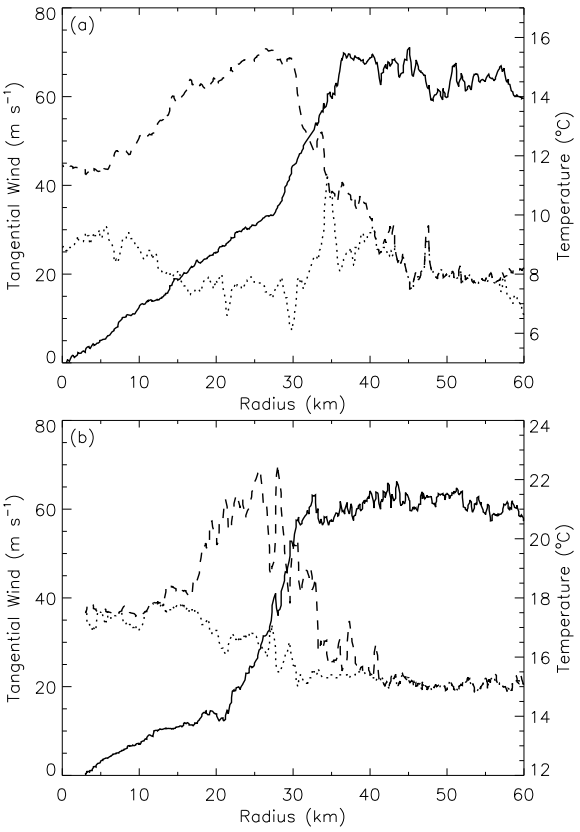

Figure 10. Radial profiles of 1 s flight-level tangential wind (solid lines), temperature (dashed lines), and dew-point temperature (dotted lines) from Hurricane Isabel on 13 September 2003 at (a) 3.7 km altitude from 1948 UTC to 1956 UTC and (b) 2.1 km altitude from 1922 UTC to 1931 UTC.

profiles for Isabel possess a striking U-shaped structure within the eye. In fact, the azimuthal wind profiles shown in Figure 10 would be more accurately characterized by a four-region model, with two regions within the eye. For example, at $z = 2.1$ km (Figure 10(b)) the average vorticity in the region $0 \leq r \leq 21$ km is 1.1×10^{-3} s^{-1}, while the average vorticity in the region $21 \leq r \leq 31$ km is 5.8×10^{-3} s^{-1}. These values result in approximate Rossby lengths for these two regions of 44 km and 8.5 km respectively. The small Rossby length in the outer part of the eye plays an important role in confining the large temperature anomaly to this region. Eye structures in which the vorticity and potential vorticity are much smaller near the circulation centre may be the result of a partial mixing process in which high-potential-vorticity eyewall air is advected inward but not completely to the centre of the eye. In passing, we note that future work should attempt to estimate temperature tendencies from large observational data sets over numerous storms to determine the robustness of the proposed relationship between inertial stability, eye subsidence and temperature tendency.

6. Conclusions

Assuming the eye can be fairly accurately characterized by a single Rossby length, we have proposed the following rules:

- There is less than 10% horizontal variation in the subsidence rate in the eye when the ratio of the eye radius to the Rossby length in the eye is less than 0.6. This tends to occur with small eyes or eyes with low inertial stability.
- The subsidence rate at the edge of the eye is more than twice as strong as the subsidence rate in the centre of the eye when the ratio of the eye radius to the Rossby length in the eye is greater than 1.8. This tends to occur with large eyes or eyes with high inertial stability.

An implication of these results is that the existence of a hub cloud at the centre of the eye, cascading pileus in the upper troposphere on the edge of the eye (Willoughby, 1998), a clear inner moat in the lower troposphere on the edge of the eye, and a warm-ring thermal structure, are all associated with strong inertial stability in the eye and a relatively large eye radius. Thus, in some cases, careful inspection of the cloud field can reveal certain aspects of a hurricane's dynamical structure. However, further research is needed to better understand the relative importance of these dynamical effects and the evaporative–sublimative cooling effects studied by Malkus (1958) and Zhang *et al.* (2002).

In closing, important limitations of the idealized framework used in this study should be pointed out. First, the balanced model (Equation (1)), and hence the associated transverse circulation equation (8), filter transient inertia–gravity waves. In real hurricanes and in both hydrostatic and non-hydrostatic primitive equation models, high-frequency inertia–gravity oscillations can be superimposed on the slower-time-scale motions that are well approximated by Equation (1). An interesting example can be seen in Yamasaki (1983, figure 15), which shows 15-minute oscillations of the vertical motion field in the eye of an axisymmetric non-hydrostatic model. Such inertia–gravity oscillations have peak amplitudes of vertical motion at the centre of the eye, in contrast to the quasi-balanced motions associated with maximum subsidence at the edge of the eye. Another interesting feature of primitive equation model simulations is that intense storms can produce a temperature field that has a warm-core structure at upper levels but a warm-ring structure at lower levels (Yamasaki, 1983, figure 10(a); Hausman *et al.*, 2006, figures 5 and 9). An explanation of such a temperature field in terms of the Sawyer–Eliassen equation would presumably involve relaxing some of the assumptions that lead to the simplified equations (9) and (10).

Acknowledgements

We would like to thank Sim Aberson, Michael Black, Paul Ciesielski, Mark DeMaria, Neal Dorst, Scott Fulton, William Gray, Richard Johnson, Kevin Mallen, Michael Montgomery, Roger Smith, Richard Taft, and an anonymous reviewer for their advice and comments. Flight-level data sets were provided by the Hurricane Research

Division (HRD) of NOAA's Atlantic Oceanographic and Meteorological Laboratory. This research was supported by NASA/TCSP Grant NNG06GA54G and NSF Grants ATM-0332197, ATM-0530884, ATM-0435694 and ATM-0435644.

References

Bell MM, Montgomery MT. 2007. Observed structure, evolution and potential intensity of category five Hurricane Isabel (2003) from 12–14 September. *Mon. Wea. Rev.* **114**: (in press).

Bundgaard RC. 1958. The first flyover of a tropical cyclone. *Weatherwise* **11**: 79–83.

Ciesielski PE, Fulton SR, Schubert WH. 1986. Multigrid solution of an elliptic boundary value problem from tropical cyclone theory. *Mon. Wea. Rev.* **114**: 797–807.

Emanuel K. 1997. Some aspects of hurricane inner-core dynamics and energetics. *J. Atmos. Sci.* **54**: 1014–1026.

Fletcher RD, Smith JR, Bundgaard RC. 1961. Superior photographic reconnaissance of tropical cyclones. *Weatherwise* **14**: 102–109.

Fulton SR, Ciesielski PE, Schubert WH. 1986. Multigrid methods for elliptic problems: A review. *Mon. Wea. Rev.* **114**: 943–959.

Gray WM, Shea DJ. 1973. The hurricane's inner core region. II. Thermal stability and dynamic constraints. *J. Atmos. Sci.* **30**: 1565–1576.

Hausman SA, Ooyama KV, Schubert WH. 2006. Potential vorticity structure of simulated hurricanes. *J. Atmos. Sci.* **63**: 87–108.

Jordan CL. 1959. A reported sea level pressure of 877 mb. *Mon. Wea. Rev.* **87**: 365–366.

Jorgensen DP. 1984. Mesoscale and convective-scale characteristics of mature hurricanes. Part II: Inner core structure of Hurricane Allen (1980). *J. Atmos. Sci.* **41**: 1287–1311.

Kossin JP, Eastin MD. 2001. Two distinct regimes in the kinematic and thermodynamic structure of the hurricane eye and eyewall. *J. Atmos. Sci.* **58**: 1079–1090.

Kossin JP, McNoldy BD, Schubert WH. 2002. Vortical swirls in hurricane eye clouds. *Mon. Wea. Rev.* **130**: 3144–3149.

Kossin JP, Schubert WH. 2001. Mesovortices, polygonal flow patterns, and rapid pressure falls in hurricane-like vortices. *J. Atmos. Sci.* **58**: 2196–2209.

Kuo HL. 1959. Dynamics of convective vortices and eye formation. In: *The Atmosphere and the Sea in Motion*, Bolin B (ed), Rockefeller Institute Press: New York, pp. 413–424.

LaSeur NE, Hawkins HF. 1963. An analysis of hurricane Cleo (1958) based on data from research reconnaissance aircraft. *Mon. Wea. Rev.* **91**: 694–709.

Malkus JS. 1958. On the structure and maintenance of the mature hurricane eye. *J. Meteor.* **15**: 337–349.

Montgomery MT, Vladimirov VA, Denissenko PV. 2002. An experimental study on hurricane mesovortices. *J. Fluid Mech.* **471**: 1–32.

Ooyama K. 1969. Numerical simulation of the life cycle of tropical cyclones. *J. Atmos. Sci.* **26**: 3–40.

Rodgers EB, Olson WS, Karyampudi VM, Pierce HF. 1998. Satellite-derived latent heating distribution and environmental influences in Hurricane Opal (1995). *Mon. Wea. Rev.* **126**: 1229–1247.

Schubert WH, Hack JJ. 1982. Inertial stability and tropical cyclone development. *J. Atmos. Sci.* **39**: 1687–1697.

Schubert WH, Montgomery MT, Taft RK, Guinn TA, Fulton SR, Kossin JP, Edwards JP. 1999. Polygonal eyewalls, asymmetric eye contraction, and potential vorticity mixing in hurricanes. *J. Atmos. Sci.* **56**: 1197–1223.

Shapiro LJ, Willoughby HE. 1982. The response of balanced hurricanes to local sources of heat and momentum. *J. Atmos. Sci.* **39**: 378–394.

Simpson RH, Starrett LG. 1955. Further studies of hurricane structure by aircraft reconnaissance. *Bull. Amer. Meteor. Soc.* **36**: 459–468.

Sitkowsi M, Dolling K, Barnes G. 2006. The rapid intensification of Hurricane Guillermo (1997) as viewed with GPS dropwindsondes. Paper 4B.8 in *Proceedings of the 27th Conference on Hurricanes and Tropical Meteorology*, 24–28 April 2006, Monterey, CA, American Meteorological Society.

Smith RK. 1980. Tropical cyclone eye dynamics. *J. Atmos. Sci.* **37**: 1227–1232.

Willoughby HE. 1998. Tropical cyclone eye thermodynamics. *Mon. Wea. Rev.* **126**: 3053–3067.

Willoughby HE, Clos JA, Shoreibah MG. 1982. Concentric eye walls, secondary wind maxima, and the evolution of the hurricane vortex. *J. Atmos. Sci.* **39**: 395–411.

Yamasaki M. 1983. A further study of the tropical cyclone without parameterizing the effects of cumulus convection. *Papers in Meteorology and Geophysics* **34**: 221–260.

Yau MK, Liu Y, Zhang D-L, Chen Y. 2004. A multiscale numerical study of Hurricane Andrew (1992). Part VI: Small-scale inner-core structures and wind streaks. *Mon. Wea. Rev.* **132**: 1410–1433.

Zhang D-L, Liu Y, Yau MK. 2002. A multiscale numerical study of Hurricane Andrew (1992). Part V: Inner-core thermodynamics. *Mon. Wea. Rev.* **130**: 2745–2763.